RESEARCH ARTICLE

Finite Element Analysis of DC Partial Discharges in Failure Types of Thin Insulation Layers in Traction Battery Systems

IVO FREUDENBERG[1,2], **THOMAS BETZ**[2], **JAN RATHGEBER**[2], **AND DANIEL HILD**[2]
[1]BMW AG, 80809 Munich, Germany
[2]Faculty of Electrical Engineering, Darmstadt University of Applied Sciences, 64295 Darmstadt, Germany

Corresponding author: Ivo Freudenberg (ivo.freudenberg@bmw.de)

ABSTRACT Improving insulation testing in traction battery systems is crucial for quality standards and the safety of passengers in electric vehicles. The DC phase resolved partial discharge diagnostics is sensible and enables information about the cause of insulation faults. Faults are referred to PRPD patterns using a DC test voltage with a superimposed AC voltage ripple as a phase reference. These patterns vary depending on the start electron location. Thus, derived models are created by analyzing defect geometries in microsections. Electric field distribution and PD activity are calculated using a time domain finite element method in combination with a stochastic tree model. The electric field distribution is mainly influenced by interfacial polarization at the surface of solid impurities. The voltage ramp and the superimposed ripple of the dc test voltage can cause partial discharges in the volume of the defect. The information about PD locations and the type of geometry of the defect can be obtained from the shape of the PD patterns. Thus, the paper results expand the knowledge about DC phase resolved partial discharge diagnostics and improve the root cause analysis of insulation faults in traction battery systems.

INDEX TERMS DC phase resolved partial discharge, finite element analysis, interfacial polarization, traction battery systems.

I. INTRODUCTION

The Intergovernmental Panel on Climate Change (IPCC) report [1] in 2022 clarifies the non-sustainable use of natural resources, destruction of ecosystems, loss of biodiversity, and social and economic inequality caused by climate change. In 2022, selling electric vehicles (EV) instead of internal combustion engine vehicles (ICEV) reduced greenhouse gas (GHG) emissions by 13 million tons [2]. However, further success of EVs in the market depends on quality standards and the safety of passengers in EVs. This challenge is crucial for increasing EVs on the road and for sustainable development in the transport sector. Especially insulation fault diagnostics for traction battery systems enhance quality and service life [3]. Early fault detection uses the DC phase resolved partial discharge (PRPD) diagnostics [4]. Partial

discharges (PDs) are a preprocess towards an electrical breakdown of the insulation system [5]. Thus, the method can be seen as an early diagnostic of insulation faults by detecting PDs. It provides PRPD patterns related to failure types of thin insulation layers in traction battery systems [4]. However, the research in DC partial discharge (PD) diagnostics is still in the early stage [6], [7]. Creating reproducible faults in thin insulation layers is a major research challenge. Thus, PD measurement investigations are supported by numerical calculations to achieve more information about the effect of geometries and different start electron locations. This paper presents a new analytical approach using a time domain finite element (FE) method [8]. For this, samples of thin insulation layers are measured by the DC PRPD method [4]. After that, defect models are derived by microsections. Furthermore, electrical fields, current, and charge density distributions of derived defect models are calculated. In addition, PD behaviors, inception,

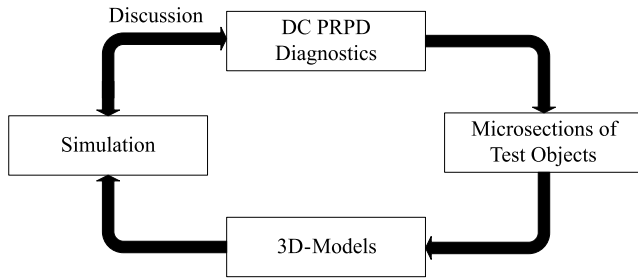The associate editor coordinating the review of this manuscript and approving it for publication was Guillaume Parent.

FIGURE 1. Overview of the research process: From DC PRPD diagnostics to simulation.

FIGURE 2. Microsections of thin PMMA insulation layers (a) Spherical Defect $r = 30.9\ \mu m$ (b) Polygonal Defect A: $l_A = 26\ \mu m$ B: $l_B = 40\ \mu m$.

and breakdown voltages are calculated using a stochastic tree model [8]. To close the loop, the simulation results are discussed and compared with the previously measured PRPD patterns to expand the knowledge about the effect of start electron locations and the PD behavior in DC systems. Hence, the objective of this paper is to determine how start electron locations in derived defects influence PD behavior in thin insulation layers at DC stress with superimposed AC ripple.

II. MODEL, METHODS AND SIMULATION PARAMETERS

Twenty samples of thin-insulated traction battery systems are tested with the DC phase resolved partial discharge (PRPD) diagnostics to identify PRPD patterns and the related failure types. After that, microsections (like Fig. 2) of the test objects are made to derive the size and geometry of selected defects using dark-field microscopy. Digital twins are created based on microsections. A novel numerical method calculates electric field, current and charge density distributions of the arrangement. Partial discharges (PDs) are also considered by enabling a stochastic tree model [8]. Finally, the simulation results are compared and discussed with the identified PRPD patterns and DC PD investigations. The discussion expands knowledge about the behavior of DC PD and the effect of the start electron locations. An overview of the research process is given in Fig. 1.

To understand the research process in detail, the following four subchapters lead through the applied methods.

A. DC PRPD DIAGNOSTICS

Compared to conventional AC partial discharge (PD) diagnostics, the PD diagnostics at DC stress remains in early stage of the research process [6], [7]. The DC phase resolved partial discharge (PRPD) diagnostics is a solution to detect and distinguish defects of thin insulation layers in traction battery systems [4]. Just like the AC PRPD method provides a phase reference, DC PRPD diagnostics feature a phase reference by a superimposed AC ripple. It was introduced by Dezenzo et al. [9] for basic high voltage arrangements and enables the creation of PRPD patterns related to different failure types. The PRPD patterns in chapter IV are measured using an Omicron MPD 800, a one-way rectification, and a test adapter with a conductive elastomer as a contact electrode. A detailed description is given in [4].
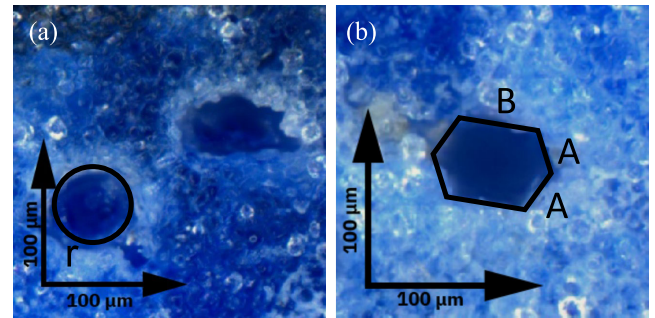
B. DEFECT MICROSECTIONS AND CREATION OF MODELS

Two defect sources have been identified in previous investigations [4]. Due to insufficient technical cleanliness of the coating process, solid impurities can be embedded in the thin polymethyl methacrylate (PMMA) insulation layer of traction battery systems. However, impurities like dust are a mixture of different materials. The defects in this paper are prepared with native corn starch to create a solid impurity with defined material properties (Fig. 2). As a second failure type, voids can be caused by an insufficient coating process, as shown in the microsections in Fig. 2. Two basic geometries of defects are derived from 20 previously tested microsections: a spherical (a) and a polygonal (b) defect. The spherical defect can be seen as a quasi-uniform arrangement. The polygonal defect has non-uniform locations. Thus, it can be analyzed as an extension compared to the spherical defect.

As a result, two digital twins of the defects are created to analyze the PD behavior at different locations in the defect. Thus, a numerical method is chosen to calculate the electric field distribution and enables the calculation of PDs.

C. NUMERICAL METHOD

Ansys Charge Plus [10] is used to calculate the distribution of electric field, current, and charge density. A quasi-static solver is applied on a finite element (FE) mesh and uses the biconjugate gradient stabilized method (BiCGSTAB) [11]. The solution is based on a simplification of the continuity equation of electrodynamics [12]

$$\frac{\delta \rho}{\delta t} + \nabla \cdot j = 0. \tag{1}$$

This simplification of the continuity equation does not consider the magnetic field caused by the current flux in the system. The presented formulation enables charge density accumulation per unit of time in the system. The formation of space charge is a common trigger for internal charging problems [10]. Ansys Charge Plus can also calculate the occurrence of PDs by enabling the electrostatic discharge (ESD) option. Thus, a stochastic tree model is implemented [8]

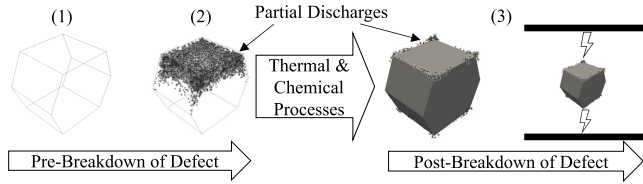$$P_i = 1 - e^{\frac{|E_i| - kE_{th}}{kE_{th}}} \tag{2}$$

FIGURE 3. Analytical approach of the stages toward total breakdown (1) Pre-Breakdown of Defect without PD (2) with PD and (3) Post-Breakdown with PD.

based on [13] to model electronic and avalanche breakdown summarized in [14] and [15]. The probability of PD P_i between two mesh elements depends on electric field magnitude $|E_i|$, breakdown threshold field magnitude E_{th}, and a breakdown element local field enhancement factor k. Decreasing the k factor from 1 to, e.g., 0.1 the PD channel (tree like formation) spreads. In this paper, the k factor is set to the default value of 0.8. As soon as PDs occur, the conductivity of the involved element is changed from intra-conductivity σ_{intra} to post-conductivity σ_{post}. The post breakdown conductivity over time influences the electric field distribution and accumulation of space charge. As a result, occurring PDs are lowering the total charge in the system [8]. The solver of Ansys Charge Plus has been validated with experimental investigations with good correlation [10].

D. ANALYTICAL APPROACH
The analysis is split into pre- and post-breakdown of the defect. Fig. 3 shows the three stages of the analytical approach.

(1) The electrical field, current, and charge density distribution of the two basic defects is analyzed to understand the stress at different defect locations.

(2) After that, partial discharges, inception voltages V_{PDIV} and breakdown voltages V_b are included in the calculation using the stochastic tree model [8]. Partial discharges and thermal and chemical processes cause electrical treeing [7] towards a carbonization of the defect. Thermal and chemical processes cannot be covered by available simulation methods.

(3) Thus, thermal, and chemical processes are excluded by analyzing a fully carbonized defect. Consequently, the approach is made to change the material property to common form of carbon (graphite). In the post-breakdown period, V_{PDIV} and V_b are calculated and determine the complete breakdown of the insulation system.

DC PRPD method requires a superimposed AC ripple. Thus, the mixed test voltage was implemented in the simulation and splited into three stages: Ramp V_{Ramp}, Ramp V_{Ramp} + DC V_{DC}, Ramp V_{Ramp} + DC with superimposed AC ripple V_{DC+AC}. The pre-breakdown stage without PD (Fig. 3 (1)) is calculated using all voltage waveforms (Fig. 4). The voltage Ramp V_{Ramp} is applied at the pre- and post-breakdown stage with PD (Fig. 3 (2),(3)) to determine V_{PDIV} and V_b.
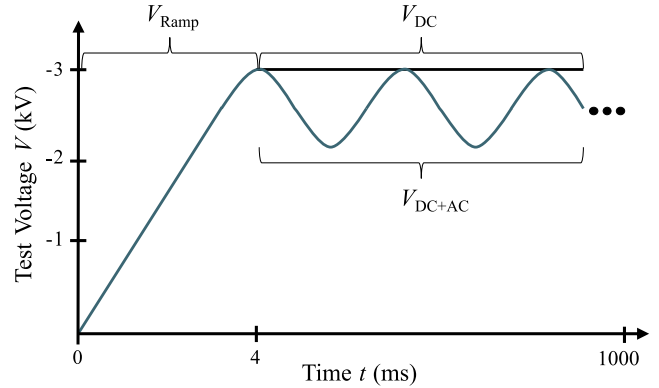

FIGURE 4. Scheme of test voltage waveforms: Ramp V_{Ramp}, Ramp V_{Ramp} + DC V_{DC}, and Ramp V_{Ramp} + DC with superimposed AC ripple V_{DC+AC}.

TABLE 1. Simulation parameters.

Symbol	Parameter	Value
t_{Ramp}	Ramp Time	4 ms
dt	Step Size	400 µs
N	Steps	2500
t_{sim}	Simulation Time	1 s
V_{max}	Maximum Absolute Voltage	-3 kV
d_g	Global Mesh Resolution	10 µm
d_d	Defect Mesh Resolution	1 µm

TABLE 2. Material properties.

Material	Conductivity σ (S/m)	Dielectric Constant ε_r	Dielectric Strength E_d (MV/m)	Mass Density ρ (kg/m^3)
PMMA	$1 \cdot 10^{-16}$ [16]	3.8 [5]	27 [17]	1180 [18]
Air	$1 \cdot 10^{-18}$ [5]	1.000589 [19]	3 [20]	1.225 [21]
Corn Starch	$5 \cdot 10^{-8}$ [22]	3 [23]	5.6	1465 [24]
Graphite	$125 \cdot 10^3$ [25]	1	-	2200 [26]

The simulation parameters (Tab. 1) are empirically evaluated based on experiments. The material properties are selected based on the literature in Tab. 2.

The simulation results are described in the following chapter.

III. SIMULATION RESULTS
A. PD LOCATIONS AT DC STRESS + AC RIPPLE
This chapter presents the simulation results of the polygonal starch defect. The polygon can be seen as an expansion compared to the spherical defect. This geometry enables the analysis of local space charge accumulation. At DC stress, the maximum electric field magnitude in defects is at the surface (Fig. 5). Additionally, the electrical field stress increases toward the edges on the surface of the defect. Fig. 5 shows the electric field distribution at the surface of a polygonal starch defect at ripple peak in steady state conditions.

After analyzing the data, four characteristic locations are chosen to plot the current density and electric field magnitude
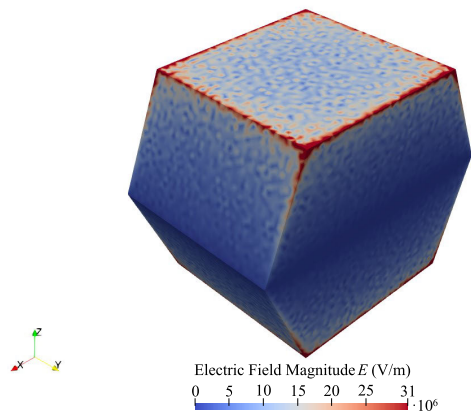
FIGURE 5. Electric field distribution of the polygonal defect at ripple peak in steady state condition (t_{sim} = 984 ms).
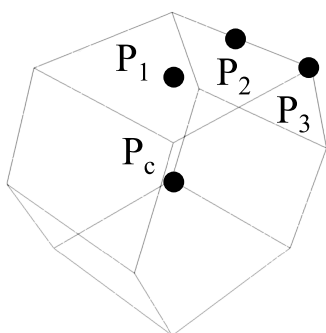

FIGURE 6. Choosen locations in the polygonal defect for plot over time analysis: P_c is in the center of the defect and P_{1-3} are located at the surface.
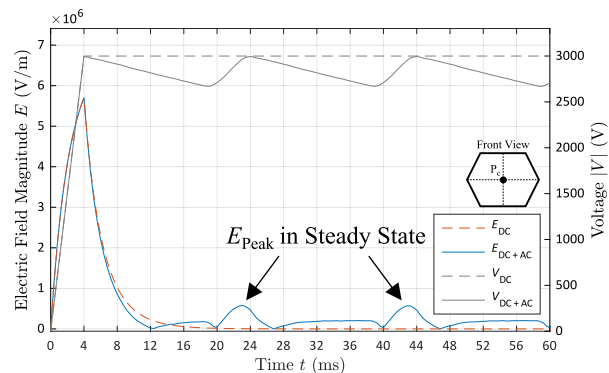

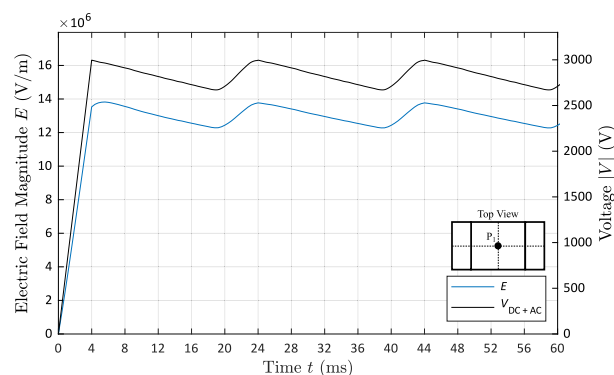**FIGURE 7.** Electric field magnitude over time $E(t)$ in the center of the defect at P_c.

FIGURE 8. Electric field magnitude over time $E(t)$ at P_1: E_{ripple} = 5.7 %, E_{max} = 13.8 · 10^6 $\frac{V}{m}$ and $\Delta\varphi$ = 0°.
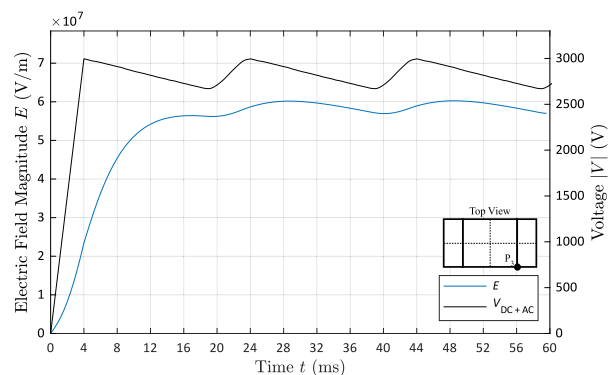

FIGURE 9. Electric field magnitude over time $E(t)$ at P_3: E_{ripple} = 2.7 %, E_{max} = 6 · 10^7 $\frac{V}{m}$ and $\Delta\varphi$ = 26°.

over time. Fig. 6 shows the analyzed locations. First, the center of the defect P_c represents a volume effect like orientation polarization. The locations P_{1-3} are at the surface of the defect. P_1 is a uniform location. P_2 is at the edge of the polygon. Moreover, P_3 is the most non-uniform location.

The following description leads through the simulation results of the locations: Orientation polarization is the primary influence factor at the center of the defect P_c. Thus, the electric field magnitude E is driven by the derivative of the applied DC and AC+DC voltages dV/dt. Fig. 7 shows the highest global electric field magnitude E during ramp time. In steady state condition the volume stress of the defect is influenced by the amplitude of the superimposed AC ripple. The spherical defect shows a similar curve shape.

It can be concluded from Fig. 5 and Fig. 7 that the highest electrical field magnitude is at the surface of the defect. In Fig. 8 the electrical field magnitude $E(t)$ follows the applied mixed voltage with a small delay at the uniform location P_1. The test voltage and electric field ripple is at 5.7 %, where E_{ripple} is

$$E_{ripple} = \frac{|E_{ripple}| - |E_{dc}|}{|E_{dc}|} 100\ \%. \tag{3}$$

P_2 and P_3 show a higher electric field magnitude up to $6 \cdot 10^7\ \frac{V}{m}$ and a lower ripple compared to the uniform location

P_1. P_3 has the maximum electrical field magnitude at the surface of the polygon (Fig. 9). However, the electric field ripple decreased to P_2: E_{ripple} = 4.5 % and P_3: E_{ripple} = 2.7 %. Thus, we assume that sharper peaks can lead to a nearly constant electric field stress. The variation of dc or mixed stress results in a change of the PD magnitude. This finding is discussed in chapter IV.

Looking at the charge density distribution (Fig. 10) indicates a capacitive effect of non-uniform defect locations.
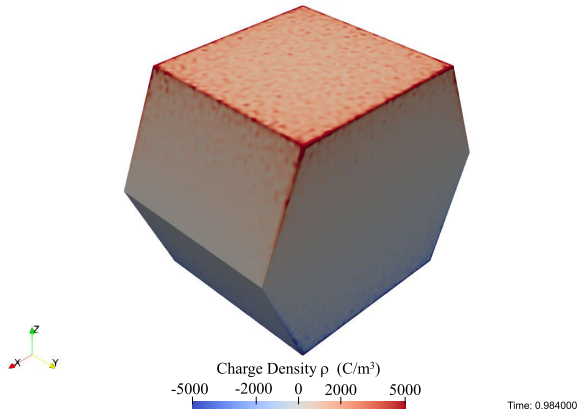
Charge Density ρ (C/m³)
-5000   -2000   0   2000   5000

Time: 0.984000

FIGURE 10. Charge density distribution of the polygonal defect at ripple peak in steady state condition ($t = 984$ ms).

Space charge formations accumulate at the surface of the solid defect. The interface charge density ρ_s is related to the Maxwell-Wagner-Sillars equation [27]:

$$\rho_s = \varepsilon_d - \varepsilon_i \frac{\sigma_d}{\sigma_i} E_d \qquad (4)$$

where ρ, ε, and E are the electric conductivity, permittivity, and electric field components of defect (d) and insulator (i).

The results show that the locations in defects are stressed differently depending on the charge density distribution and the geometry of the defect. More non-uniform areas or defects are stressed with lower ripple compared to the applied test voltage due to a capacitive damping effect of the local accumulated charge. Thus, the PD activity depends on the electric field stress of the start electron location. The maximum electric field stress of the locations is sorted $\hat{E}_{P_c} < \hat{E}_{P_1} < \hat{E}_{P_2} < \hat{E}_{P_3}$. Furthermore, the PD activities of the spherical and polygonal defect are described, and key figures are calculated.

B. PD BEHAVIOR OF TWO DEFECT GEOMETRIES

In this chapter, the voltage V_{Ramp} (Fig. 4) is applied to calculate the PD inception voltage $|V_{\text{PDIV}}|$ and the breakdown voltage $|V_b|$ of the defects using the stochastic tree model [8]. $|V_b|$ is defined as the full coverage of the object where PD activity occurs. The results, depending on different material properties, are summarized in Tab. 3, 4. The spherical defect can be seen as a quasi-uniform geometry. Thus, $|V_b|$ and $|V_{\text{PDIV}}|$ are at higher voltages compared to the non-uniform polygonal defect. The PD activity time between $|V_{\text{PDIV}}|$ and $|V_b|$ of the spherical defect is relatively short (Tab. 3). That indicates a fast breakdown of the system. Once the PD activity is intense enough to completely carbonize the defect, breakdown of the insulation system is imminent. Non-uniform defects like polygonal defects show early PD activity. If the polygonal defect is filled with air, the virtual defect fails immediately. However, in this calculation, the probability of a free electron to start an avalanche, is not implemented. Thus, these air inclusions are assumed to be

TABLE 3. Spherical defect: PD quantities.

Quantity	Air	Starch	Graphite
$|V_{\text{PDIV}}|$ (V)	479.03	1997.26	1671.76
$|V_b|$ (V)	479.05	1997.27	1672.55
t_{PDIV} to t_b (s)	$3 \cdot 10^{-8}$	$2 \cdot 10^{-8}$	$1.06 \cdot 10^{-6}$

TABLE 4. Polygonal defect: PD quantities.

Quantity	Air	Starch	Graphite
$|V_{\text{PDIV}}|$ (V)	324.30	595.50	1207.51
$|V_b|$ (V)	324.32	979.07	1208.30
t_{PDIV} to t_b (s)	$3 \cdot 10^{-8}$	$5.11 \cdot 10^{-4}$	$1.06 \cdot 10^{-6}$

able to provide a start electron. Regarding this defect material, the calculation can be improved using an FDTD method [28] with non-linear air chemistry [29], [30]. The maximum PD activity time is at the polygonal starch defect. This defect is suitable to show PD development over time.

Fig. 11 shows the PD development over time. The first PD occurs at the corner of the polygon. In the next time steps, the PDs show avalanche behavior and move along the edges of the polygonal defect. Consequently, PDs move into the defect until a critical number of PDs is reached. After that, PDs move further along the edges. The polygonal defect is fully filled with PD activity by repeating this process.

After this valuable information about electric field distributions and PD behaviors, this paper discusses the findings and compares them with the PD measurements of the samples. The aim is to derive additional information about the PD location using the phase reference.

IV. DISCUSSION

The discussion chapter compares the simulation results with the measured PRPD patterns. The discussion shows similarities and extends the knowledge about the PD behavior of the DC PRPD method.

A. CAPACITIVE EFFECT ON DIFFERENT PD LOCATIONS

In chapter III the simulation results show different field stress depending on the location of the start electron (Fig. 6). The non-uniform geometry of the polygonal starch defect is suitable for discrete analysis, since the PD does not lead to immediate breakdown.

For the following analysis, it is assumed, that a start electron is available at P_c. In this case, the AC ripple mainly stresses the defect. Fig. 12 (a) shows a measured hill-shaped PD pattern corresponding to the electrical field stress displayed in Fig. 12 (b). Fig. 12 (b) is a close-up view to E_{peak} in steady state conditions (cf. Fig. 7). The rise of the hill-shaped PD pattern in Fig. 12 (a) is steeper than the fall. In comparison to the electric field curve in Fig. 12 (b), the shape is similar.

However, the start electron probability in the defect's center is low due to the relatively low electric field magnitude
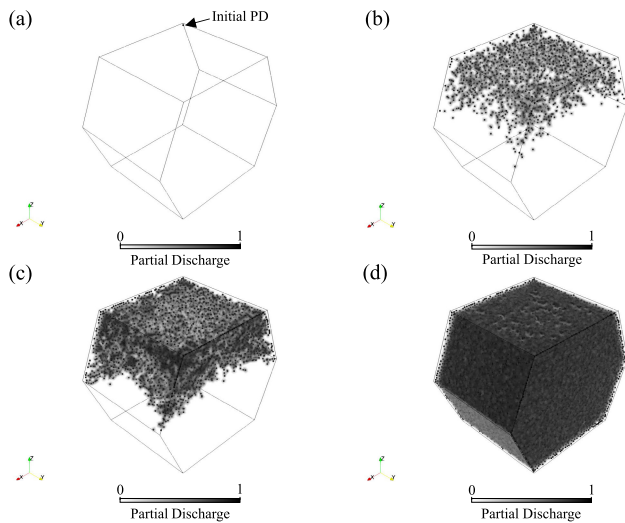
FIGURE 11. PD behavior at different time steps (a) PDIV $V_{PDIV} = -595.50$ V (b) $V = -595.52$ V (b) $V = -603.01$ V (d) $V = -979.07$ V.

compared to the electric field stress at the surface of the defect. That indicates that the voltage ramp triggers volume PD activity. The hill-shaped electric field stress is higher than the extinction field magnitude, i.e., in the range of the hysteresis of PD activity. PD investigations show that the hill-shaped pattern starts directly after the voltage ramp. If the voltage ripple in Fig. 12 is reduced to 0.4 %, the hill-shaped pattern disappears at the PRPD diagram, and the extinction field stress is reached.

It is now assumed that a start electron is available at P_1. The ripple of the electric field magnitude (Fig. 13 (b)) forms the plateau-shaped PD patterns in Fig. 13 (a). Two plateau-shaped PD patterns can be identified depending on the PD inception of the uniform location at the surface of the defect.

In Figure 13 (a), there are two patterns shown. The first pattern (1) displays a continuous plateau-shaped PD formation, while the second pattern (2) shows a sectional plateau-shaped PD formation over the phase angle. The variation depends on the electric field stress and strength of the location. If the electric field stress is higher than the electric strength of the PD location, the PDs occur throughout the entire period. However, if the electric field stress and strength cross, the plateau-shaped PD pattern appears in sections. Fig. 14 visualizes the variation of the plateau-shaped PD pattern by electric field strengths E_{PDIV1} and E_{PDIV2} that refers to the measured PD patterns (1), and (2) in Fig. 13 (a). These findings are comparable with [31], where different PD inception voltages in a void result in varying PD activity at DC+AC stress.

However, the PD patterns are not in a steady state condition. The sectional plateau-shaped patterns can develop throughout the entire period over time due to PD activity and the changing conductivity. It is also possible that this change in conductivity leads to local non-uniform electric field distribution. Consequently, the phase related plateau-shaped
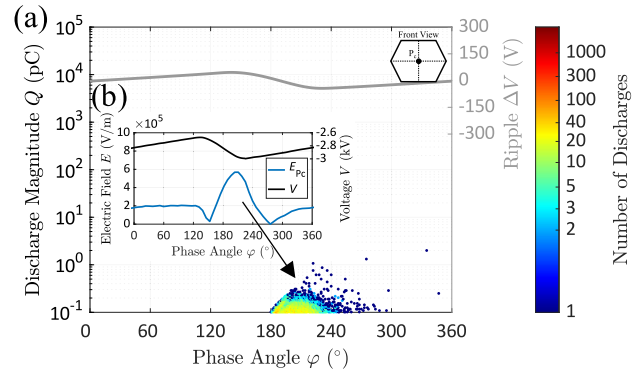

FIGURE 12. Electrical field magnitude forms (a) hill-shaped PRPD pattern at P_C, (b) electric field magnitude peak at phase angle $\varphi = 210°$ as hill-shaped PD peak.
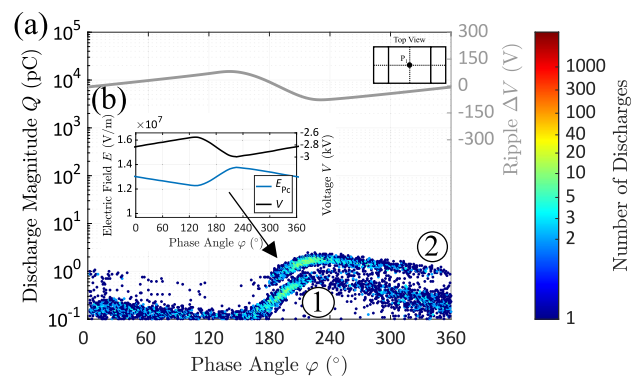

FIGURE 13. Electrical field magnitude forms (a) plateau-shaped PRPD patterns (1) continuous and (2) in sections at P_1, (b) electric field magnitude $E(\varphi)$ at P_1.
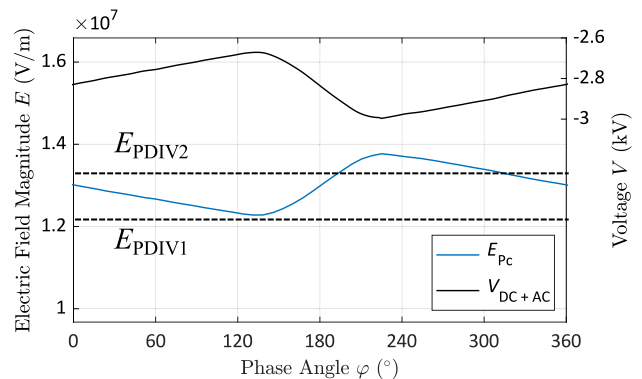

FIGURE 14. Two PDIV locations with different electric field strength: E_{PDIV1} refers to lower continuous plateau-shaped PD pattern in Fig. 14 (a1), E_{PDIV2} refers to upper sectional plateau-shaped PD pattern in Fig. 14 (a2).

pattern develops into a constant plateau. This effect acts equally as a start electron at the corner of the polygon at P_3. Thus, the PD activity forms a constant plateau-shaped pattern (Fig. 15 (a)) due to the low ripple of electrical field magnitude in this location (Fig. 15 (b)). Comparable to Fig. 14, the constant plateau can rarely occur in sections if the E_{PDIV} has not entirely exceeded the local electric field strength.

The electric field stress at the corner of the polygon is the global maximum of the defect. Thus, the probability of a start
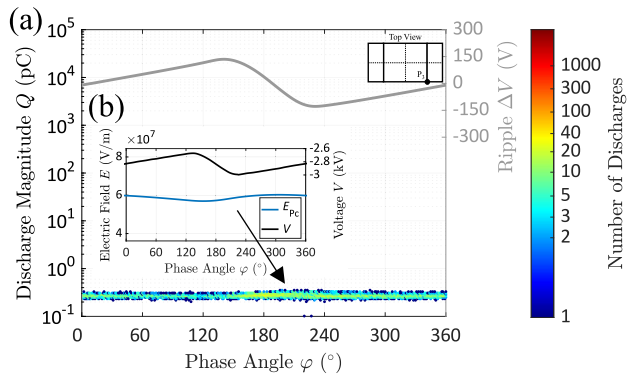
FIGURE 15. Electrical field magnitude forms (a) constant plateau-shaped PRPD pattern at P_3 (b) electric field magnitude $E(\varphi)$ at P_3.

electron due to the accumulated charge is higher than in other locations. As a result, the constant plateau-shaped PD pattern is the most identified pattern. In the following chapter, the simulation considers PD activity and the results are compared with the findings of our DC PD investigations.

B. INCEPTION AND BREAKDOWN VOLTAGE

Impurities are identified as the leading cause of PD activity with DC stress. Interface polarization triggers high electric field stress and the accumulation of charge. Most of the time, impurities in operation are accumulations of particles. Thus, the probability of non-uniform defect geometries is high. Consequently, solid discharges can be measured until the particles are carbonized, and the thin insulation system fails. The solid discharges on the defect surface lead to a plateau-shaped PD pattern. It is the most frequently encountered pattern. This pattern was found to be critical for the insulation system, as confirmed by previous research. The start of calculated PD activity is always located at one corner of the polygonal starch defect. As soon as an electron starts at the corner of the polygonal defect, an avalanche behavior like in [4] could be observed. The time until the solid discharge leads to a breakdown of the insulation system varies depending on the unique geometry and local field stress of the impurity. However, if the defect is carbonized, it fails immediately at the applied voltage of 3 kV. This finding was confirmed by measurements using metal particles. Defects filled with air have the lowest inception voltage V_{PDIV}. The calculated inception voltages V_{PDIV} do not match our PD measurements as the probability of start electron at DC stress is not considered. Electric field and PD calculation in voids can be improved using a time domain FDTD method [28] with non-linear air chemistry [29], [30].

V. CONCLUSION

The paper provides information about the starting location of PD activity depending on the local field stress. From now on, it is possible to refer patterns to failure types. Moreover, the shape of the plateau pattern (solid discharges) provides information about the uniformity of the local electric field

stress. Additionally, the hill-shaped pattern could be assigned to volume PD activity. This information about the condition of thin insulation layers in traction battery systems leads to early fault detection by identifying the root cause of the failure. Failure cause information can also be used to reflect insulation processes and the assembly of traction battery systems. Moreover, PD diagnostics of stationary battery systems should be considered, depending on the operating voltage and thickness of the insulation system.

In future work, combined faults will be simulated to analyze the electric field stress caused by accumulated impurities. Especially the superimposition of space charge between defect particles are assessed as a critical stress for the insulation system.

REFERENCES

[1] *Climate Change 2022: Impacts, Adaptation, and Vulnerability: Contribution of Working Group II to the Sixth Assessment Report of the Intergovernmental Panel on Climate Change*, IPCC, Geneva, Switzerland, 2022.

[2] *CO$_2$ Emissions in 2022*, International Energy Agency (IEA), Paris, France, 2022.

[3] R. Xiong, W. Sun, Q. Yu, and F. Sun, "Research progress, challenges and prospects of fault diagnosis on battery system of electric vehicles," *Appl. Energy*, vol. 279, Dec. 2020, Art. no. 115855.

[4] I. Freudenberg, T. Betz, S. Gillilan, and D. Hild, "Early fault detection of thin insulation layers in traction battery systems using DC partial discharge diagnostics," in *Proc. VDE High Voltage Technol. (ETG-Symp.)*, Nov. 2022, pp. 1–6.

[5] A. Küchler, *High Voltage Engineering*. Berlin, Germany: Springer, 2018.

[6] J. Guo, Z. Zheng, and A. Caprara, "Partial discharge tests in DC applications: A review," in *Proc. IEEE Electr. Insul. Conf. (EIC)*, Jul. 2020, pp. 225–229.

[7] C. Li, T. Shahsavarian, M. A. Baferani, K. Davis, Y. Cao, and D. Thang, "Understanding of DC partial discharge: Recent progress, challenges, and outlooks," *CSEE J. Power Energy Syst.*, vol. 8, no. 3, pp. 894–909, 2021.

[8] G. Wilson, B. Neufeld, and K.-D. Merenda, "Dielectric breakdown simulations using a stochastic tree model," NASA, Tech. Rep., pp. 1–19, 2021.

[9] T. Dezenzo, T. Betz, and A. Schwarzbacher, "Phase resolved partial discharge measurement at DC voltage obtained by half wave rectification," in *Proc. VDE High Voltage Technol. (ETG-Symp.)*, Nov. 2018, pp. 1–6.

[10] K.-D. Merenda, B. Neufeld, G. Wilson, and T. McDonald, "Spacecraft charging with EMA3D charge," *Adv. Space Res.*, vol. 1, Mar. 2023. [Online]. Available: https://www.sciencedirect.com/science/article/abs/pii/S0273117723002156

[11] G. L. Sleijpen and D. R. Fokkema, "BiCGstab(ℓ) for linear equations BiCGstab(ℓ) for linear equations involving unsymmetric matrices with complex spectrum," *Electron. Trans. Numer. Anal.*, vol. 1, pp. 11–32, Sep. 1993.

[12] R. A. Wildman and G. A. Gazonas, "A multiphysics finite element and peridynamics model of dielectric breakdown," U.S. Army Res. Lab., Adelphi, MD, USA, Tech. Rep. ARL-TR-8128, 2017.

[13] H. J. Wiesmann and H. R. Zeller, "A fractal model of dielectric breakdown and prebreakdown in solid dielectrics," *J. Appl. Phys.*, vol. 60, no. 5, pp. 1770–1773, Sep. 1986.

[14] T. L. Skvarenina, *An Introduction to Electrical Breakdown in Dielectrics*. Maxwell Air Force Base, Alabama: ACSC/EDCC, 1985.

[15] L. Zhao, "A formula to calculate solid dielectric breakdown strength based on a model of electron impact ionization and multiplication," *AIP Adv.*, vol. 10, no. 2, Feb. 2020, Art. no. 025003.

[16] W. Zheng and S.-C. Wong, "Electrical conductivity and dielectric properties of PMMA/expanded graphite composites," *Compos. Sci. Technol.*, vol. 63, no. 2, pp. 225–235, Feb. 2003.

[17] *Plexiglas® GS/XT: Technische Information*, Röhm GmbH, 2020.

[18] W. Kaiser, *Kunststoffchemie für Ingenieure: Von der Synthese bis zur Anwendung*, 3 ed. München, Germany: Hanser, 2011.

[19] L. G. Hector and H. L. Schultz, "The dielectric constant of air at radiofrequencies," *Physics*, vol. 7, no. 4, pp. 133–136, Apr. 1936.

[20] J. S. Rigden, *Macmillan Encyclopedia of Physics*. New York, NY, USA: Macmillan, 1996.

[21] *Luftdichte*, DWD, 2023.

[22] C. Y. Beh, E. M. Cheng, N. F. M. Nasir, M. S. A. Majid, S. F. Khor, M. R. M. Jamir, E. Z. M. Tarmizi, and K. Y. Lee, "Dielectric properties of hydrothermally modified potato, corn, and rice starch," *Agriculture*, vol. 12, no. 6, p. 783, May 2022.

[23] P. Ramasamy, "A dielectric relaxation study of starch–water and starch–glycerol films," *Ionics*, vol. 18, no. 4, pp. 413–423, Apr. 2012.

[24] *Produktinformation—Product Information: Esstar Stäube—Esstar Dusts*, KSL Staubtechnik GmbH, Lauingen, Germany 2022.

[25] H. Czichos and M. Hennecke, *HÜTTE—Das Ingenieurwissen*. Berlin, Germany: Springer, 2012.

[26] N. Wiberg, *Grundlagen und Hauptgruppenelemente: Band 1: Grundlagen und Hauptgruppenelemente. De Gruyter Paket Physik, Chemie, Industrielle Chemie, Materialwissenschaft, Geowissenschaften*, vol. 103. Berlin, Germany: De Gruyter, 2017.

[27] J. C. Maxwell, *A Treatise on Electricity and Magnetism*, 1st ed. Oxford, U.K.: Clarendon Press, 1873.

[28] K. Yee, "Numerical solution of initial boundary value problems involving maxwell's equations in isotropic media," *IEEE Trans. Antennas Propag.*, vol. AP-14, no. 3, pp. 302–307, May 1966.

[29] T. Rudolph and R. A. Perala, "Linear and nonlinear interpretation of the direct strike lightning response of the NASA F106B thunderstorm research aircraft," NASA Sci. Tech. Inf. Branch, Denver, CO, USA, Tech. Rep. 3746, 1983.

[30] T. Rudolph, R. A. Perala, C. C. Easterbrook, and S. L. Parker, "Development and application of linear and nonlinear methods for interpretation of lightning strikes to in-flight aircraft," NASA Sci. Tech. Inf. Branch, Denver, CO, USA, Tech. Rep. 3974, 1986.

[31] M. Florkowski, M. Kuniewski, and P. Zydron, "Partial discharges in HVDC insulation with superimposed AC harmonics," *IEEE Trans. Dielectr. Electr. Insul.*, vol. 27, no. 6, pp. 1906–1914, Dec. 2020.

THOMAS BETZ received the Dr.-Ing. (Ph.D.) degree from the Technical University of Darmstadt, in 1997. He has 11 years industrial experience in development of high voltage gas-insulated switchgear, finally as the head of development. In 2009, he joined the Darmstadt University of Applied Sciences as a Professor in high voltage technology and power systems. He is currently a member of VDE and Cigré. In this context he participated in the Cigré working group A3.27 about the impact of the application of vacuum switchgear at transmission voltages. His research interests include defect prevention by partial discharge analysis and the recognition of failure causes in case of DC-applications.
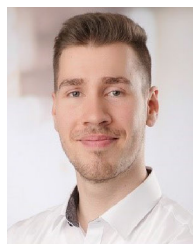
JAN RATHGEBER received the B.Eng. and M.Sc. degrees from the Darmstadt University of Applied Sciences, Germany in 2021 and 2023, respectively.

IVO FREUDENBERG was born in Heidelberg, Germany, in 1995. He received the B.Eng. and M.Sc. degrees in electrical engineering from the Darmstadt University of Applied Sciences, Germany, in 2019 and 2020, respectively, where he is currently pursuing the Ph.D. degree with the Doctoral Center of Sustainability Sciences. He is also a participant of the BMW Group Ph.D. Program. His current research interests include automotive test technologies, partial discharges at DC voltage, and the sustainability assessment of technologies.

DANIEL HILD received the B.Eng. and M.Sc. degrees from the University of Applied Sciences Darmstadt, Germany, in 2020 and 2022, respectively. He is currently a Research Assistant with the Darmstadt University of Applied Sciences.

• • •